JGR Space Physics

RESEARCH ARTICLE
10.1029/2019JA027665

Magnetic Reconnection Inside a Flux Rope Induced by Kelvin-Helmholtz Vortices

K.-J. Hwang[1], K. Dokgo[1], E. Choi[1], J. L. Burch[1], D. G. Sibeck[2], B. L. Giles[2], H. Hasegawa[3], H. S. Fu[4], Y. Liu[4], Z. Wang[4], T. K. M. Nakamura[5], X. Ma[6], R. C. Fear[7], Y. Khotyaintsev[8], D. B. Graham[8], Q. Q. Shi[9], C. P. Escoubet[10], D. J. Gershman[2], W. R. Paterson[2], C. J. Pollock[11], R. E. Ergun[12], R. B. Torbert[13], J. C. Dorelli[2], L. Avanov[2,14], C. T. Russell[15], and R. J. Strangeway[15]

[1]Southwest Research Institute, San Antonio, TX, USA, [2]NASA Goddard Space Flight Center, Greenbelt, MD, USA, [3]Institute of Space and Astronautical Science, Japan Aerospace Exploration Agency, Sagamihara, Japan, [4]School of Science and Environment, Beihang University, Beijing, China, [5]Austrian Academy of Sciences ÖAW, Space Research Institute, Graz, Austria, [6]Physical Sciences Department, Embry-Riddle Aeronautical University, Daytona Beach, FL, USA, [7]School of Physics and Astronomy, University of Southampton, Southampton, UK, [8]Swedish Institute of Space Physics, Uppsala, Sweden, [9]School of Earth and Space Sciences, Peking University, Peking, China, [10]European Space Research and Technology Centre, Noordwijk, the Netherlands, [11]Denali Scientific, LLC, Fairbanks, AK, USA, [12]Laboratory for Atmospheric and Space Physics, University of Colorado at Boulder, Boulder, CO, USA, [13]Space Science Center, University of New Hampshire, Durham, NH, USA, [14]The Goddard Planetary Heliophysics Institute, University of Maryland, Baltimore County, Baltimore, MD, USA, [15]Institute of Geophysics and Planetary Physics, University of California, Los Angeles, Los Angeles, CA, USA

Key Points:
- MMS observed a magnetic flux rope formed on the boundary of a nonlinear Kelvin-Helmholtz (KH) wave
- Both in-plane and midlatitude reconnection associated with the 3-D structure of the KH vortex-inducedflux rope were identified
- A current sheet at the flux rope center supported by reconstruction indicates two flux tubes interlinked to form a crater-type flux rope

Supporting Information:
- Supporting Information S1

Correspondence to:
K.-J. Hwang,
jhwang@swri.edu

Citation:
Hwang, K.-J., Dokgo, K., Choi, E., Burch, J. L., Sibeck, D. G., Giles, B. L., et al. (2020). Magnetic reconnection inside a flux rope induced by Kelvin-Helmholtz vortices. *Journal of Geophysical Research: Space Physics*, *125*, e2019JA027665. https://doi.org/10.1029/2019JA027665

Received 20 NOV 2019
Accepted 3 MAR 2020
Accepted article online 25 MAR 2020

Abstract On 5 May 2017, MMS observed a crater-type flux rope on the dawnside tailward magnetopause with fluctuations. The boundary-normal analysis shows that the fluctuations can be attributed to nonlinear Kelvin-Helmholtz (KH) waves. Reconnection signatures such as flow reversals and Joule dissipation were identified at the leading and trailing edges of the flux rope. In particular, strong northward electron jets observed at the trailing edge indicated midlatitude reconnection associated with the 3-D structure of the KH vortex. The scale size of the flux rope, together with reconnection signatures, strongly supports the interpretation that the flux rope was generated locally by KH vortex-induced reconnection. The center of the flux rope also displayed signatures of guide-field reconnection (out-of-plane electron jets, parallel electron heating, and Joule dissipation). These signatures indicate that an interface between two interlinked flux tubes was undergoing interaction, causing a local magnetic depression, resulting in an M-shaped crater flux rope, as supported by reconstruction.

Plain Language Summary Magnetic reconnection and Kelvin-Helmholtz instability (KHI), two of the most fundamental physical processes occurring within the heliosphere and throughout the Universe, often occur simultaneously on the Earth's magnetopause. Previous studies indicate the importance of nonlinearly developed KH waves, which produce multiple kinetic layers facilitating reconnection both in and out of the velocity shear plane and resulting in the magnetic flux rope. However, these studies significantly lacked detailed in situ observations in quantity as well as appropriate 3-D analyses of the structure of the KH vortex-induced flux rope. In this paper, we use detailed observations by the MMS spacecraft to investigate both 2-D and 3-D structures of the flux rope developed along the KH waves. We found that two flux tubes interact through reconnection to form a single combined structure, which can explain the occurrence of M-shaped crater flux rope.

1. Introduction

Magnetic reconnection and the Kelvin-Helmholtz instability (KHI) are two of the most fundamental physical processes occurring within the heliosphere and throughout the Universe. The former is facilitated by large magnetic field shear, and the latter is by large flow velocity shear. Both processes, being important in the solar wind-magnetosphere coupling, exhibit multiscale features involving large-scale structures that magnetohydro-dynamics can describe, the smaller ion diffusion region where Hall physics resulting from demagnetized ions governs the magnetofluid description, and the smallest electron diffusion region (EDR) where the electron physics dominates over the fluid and Hall physics.

Observations and simulations often indicate the simultaneous occurrence of reconnection and Kelvin-Helmholtz waves (KHWs) on the Earth's magnetopause. 2-D magnetohydro-dynamic simulations (Nykyri & Otto, 2001; Otto & Fairfield, 2000) together with comparisons with Geotail observations (Fairfield et al., 2000) indicated that local reconnection between stretched magnetic field lines caused by the vortex motion lead to the injection of magnetosheath-origin plasmas across the flank magnetopause. Eriksson et al. (2009) reported THEMIS observations of a magnetic island on a scale size less than 0.56 R_E (Earth radii) that formed at the trailing (i.e., sunward) edge of KHWs. 2-D and 3-D kinetic simulations showed that Kelvin-Helmholtz vortices (KHVs), i.e., the nonlinearly developed structure of KHWs (Hasegawa et al., 2004), drive the onset of reconnection and the generation of flux ropes, as highly stretched field lines and compressed current sheet layers form within the vortices (Nakamura et al., 2011, 2013). Nakamura, Eriksson, et al. (2017) and Nakamura, Hasegawa, et al. (2017) used large-scale 3-D kinetic simulations to investigate the evolution of vortex-induced reconnection (VIR). Via comparison with MMS observations (Eriksson, Lavraud, et al., 2016; Eriksson, Wilder, et al., 2016), they showed a series of flux ropes developing along the vortex boundary and their coalescence and decay forming a turbulent layer, which facilitates a mass transfer across the magnetopause.

KHVs induce reconnection occurring not only in the velocity shear plane at the low-latitude (near the equatorial plane) flank of the Earth's magnetopause. Takagi et al. (2006) proposed dual reconnection between KHI-stable lobe fields and vortex-induced engulfed magnetosheath fields (figure 12 of Takagi et al., 2006). Faganello, Califano, Pegoraro, Andreussi, and Benkadda (2012) termed a similar mechanism as midlatitude reconnection, which, however, involves closed pristine magnetospheric fields (blue lines in figure 1 of Faganello et al., 2012; blue in figure 3r) and engulfed magnetosheath fields (red lines in figure 1 of Faganello et al., 2012; black in figure 3r) due to a three-dimensional (3-D) distortion/twist of the field lines between the low-latitude flank magnetopause (that is unstable to KHI) and higher latitude flank magnetopause (stable to KHI). Vernisse et al. (2016) categorized various magnetic field topologies that can arise within KHWs via midlatitude and/or low-latitude (in-plane) reconnection into seven types (figure 2 of Vernisse et al., 2016). They used electron and ion pitch angle distributions together with in-plane outflow jet signatures (when existing) to distinguish different magnetic field connections. For example, observations of unidirectional field-aligned electrons are expected for one end of the magnetosheath field line connected at one midlatitude reconnection site, i.e., parallel (antiparallel) electrons for a reconnection site at southern (northern) midlatitudes.

While these studies indicate the importance of KHVs, which produce multiple kinetic layers facilitating reconnection both in and out of the velocity shear plane and kinetic physics regarding the VIR and flux ropes, we lack detailed in situ observations and appropriate 3-D analyses of the structure of the VIR-induced flux rope. In this paper, we report a flux rope observed on the boundary layer of nonlinear KHWs at the dawnside tailward magnetopause. At the leading and trailing edges of the flux rope, signatures of not only VIR occurring in the plane of the velocity shear but also midlatitude reconnection occurring in the Southern Hemisphere were identified. In addition, the central current sheet of the flux rope exhibited signatures of strong guide-field reconnection, suggesting an interacting interface of the two interlaced flux tubes (Kacem et al., 2018; Øieroset et al., 2019). We present the first fully kinetic 2–1/2-dimensional simulation of the VIR induced at the dawnward magnetopause to compare with the MMS observation. Using reconstruction techniques, we investigate both 2-D and 3-D structures of the VIR-induced flux rope and discuss the kinetic processes occurring within the flux rope that possibly lead to the formation of an "M-shaped crater flux rope."

2. Overview of the Event

Over ~4 hr from 1920 to 2320 UT on 5 May 2017, the MMS quartet (Burch, Moore et al., 2016) observed quasi-periodic perturbations of the dawnside tailward magnetopause. Figure 1 shows upstream solar wind conditions obtained from ACE OMNI-HRO 1-min data (Figures 1a–1c: magnetic field, velocity, and dynamic pressure), downstream dayside/dawnside magnetosheath properties observed by Cluster-4 (Figures 1d–1g: magnetic field, ion velocity, ion density, and plasma (red), magnetic (blue), dynamic (green) pressures, and the sum (black) of these pressures), and dawnside tailward magnetopause boundary layer behavior encountered by MMS4 (Figures 1h–1n: magnetic field—x, y, and z components with the

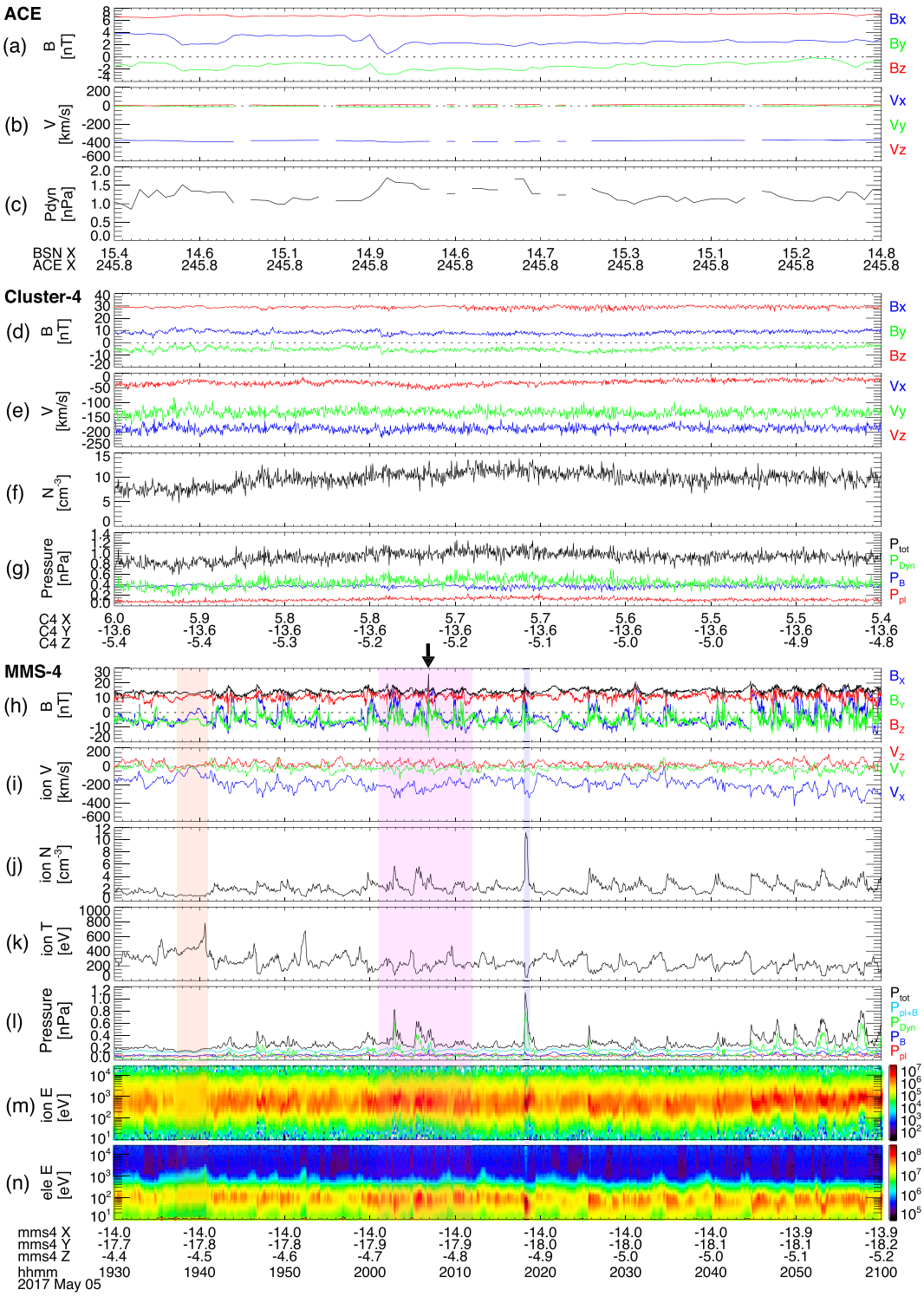

Figure 1. (a–c) ACE observation of upstream solar wind conditions (OMNI-HRO 1-min resolution data): (a) Magnetic field, (b) velocity, (c) and dynamic pressure. (d–g) Cluster-4 observation of downstream dayside/dawnside magnetosheath: (d) magnetic field, (e) ion velocity, (f) ion density, and (g) plasma (red), magnetic (blue), dynamic (green) pressures, and the sum (black) of these pressures. (h–n) MMS observation of dawnside tailward magnetopause boundary layer: (h) the *x*, *y*, and *z* (blue, green, and red) components magnetic field with the magnetic strength (black), (i) ion velocity, (j) ion density, (k) ion temperature, (l) plasma (red), magnetic (blue), dynamic (gree) pressures, the sum of plasma and magnetic pressures (cyan) and the sum of all three pressures (black), (m) ion energy spectrogram, and (n) electron energy spectrogram).

magnetic strength (black), ion velocity, ion density, ion temperature, pressures, ion energy spectrogram, and electron energy spectrogram) from 1930 UT to 2100 UT. The ACE HRO data provide the time-shifted interplanetary magnetic field (IMF) and solar wind parameters at a model bow shock nose location (Farris & Russell, 1994). All vector parameters in Figure 1 are shown in Geocentric Solar Magnetospheric (GSM) coordinates (see Supporting Information S1, for the description about the MMS instruments used for the present study).

The event occurred within a period of mainly northward and slightly sunward/dawnward IMF (Figures 1a and 1d). The magnetic field, plasma density, and temperature (Figures 1h–1k) at/near the dawnward/tailward magnetopause exhibit quasi-periodic fluctuations with a period of ~2.5–6 min (details to be shown in Figure 2). Neither upstream solar wind (dynamic pressure, in particular; Figure 1c) nor downstream magnetosheath (velocity or dynamic pressure; Figures 1e and 1g) displays such quasi-periodic fluctuations observed by MMS4 throughout the interval shown in Figure 1. This strongly indicates that the magnetopause boundary layer fluctuations observed by MMS4 resulted from surface waves instead of solar wind/magnetosheath-driven undulations.

During the 1.5 hr (Figure 1), MMS4 made a short excursion to the magnetosphere (denoted by the red shading in Figures 1h–1n from ~1937 to 1941 UT) and the magnetosheath (the blue shading from ~2018 to ~2019 UT). Note the absence or reduction in high-energy (e.g., >10 keV) ion populations during the magnetosphere crossing, which is a common feature of the dawnside low-latitude boundary layer and plasma sheet under northward IMF (Wing et al., 2005). The data averaged from 1939 to 1941 UT for the magnetospheric side ("1") and from 2018:05 to 2018:40 UT for the magnetosheath side ("2") well satisfy the threshold condition for the nonlinear KHW, $[\mathbf{k}\cdot(\mathbf{V}_2-\mathbf{V}_1)]^2 > \frac{1}{\mu_0}\left(\frac{1}{\rho_1}+\frac{1}{\rho_2}\right)\left[(\mathbf{B}_1\cdot\mathbf{k})^2+(\mathbf{B}_2\cdot\mathbf{k})^2\right]$ (Hasegawa, 1975; where $\mathbf{V}_{1,2}$, $\rho_{1,2}$, and $\mathbf{B}_{1,2}$ represent flow velocity, plasma density and magnetic field at sides 1 and 2, respectively), assuming that the $\mathbf{k}$ vector of the KHW is directed antisunward. However, testing this condition tells whether or not the velocity shear layer is unstable to KHI at the time of the observation, rather than the observed surface wave is a nonlinear KHW or not. To confirm the latter point, we further performed boundary normal analysis for a few cycles of these fluctuations denoted by the magenta shading in Figures 1h–1n (detailed in following paragraphs). This period includes a unique signature of a magnetic strength peak marked by the black arrow at the top of Figure 1h.

Figure 2 shows the detailed field and plasma signatures during an 11-min interval starting from 2001 UT (the magenta shading in Figures 1h–1n), observed by MMS4 located at ~(−14, −18, −4.8) Earth radii (R_E) in GSM. The four MMS spacecraft were in a tetrahedron with an average separation of 156 km, comparable to the ion inertial length (75~125 km on the magnetosheath side and 200~275 km on the magnetospheric side). All vector parameters in Figure 2 are shown in GSM. The top panel (Figure 2a) shows the x (blue), y (green), and z (red) components of the magnetic field ($\mathbf{B}$). The color-coded ion (Figure 2b) and electron (Figure 2c) energy spectrograms are followed by the ion density (Figure 2d), bulk velocity (Figure 2e), and temperature (Figure 2f). Figure 2g shows the plasma (red) and magnetic (blue) pressures and the sum of plasma and magnetic pressures (black).

The magnetic field, ion energy spectrogram, plasma density, and temperature (Figures 2a, 2b, 2d, and 2f) show the quasi-periodic fluctuation. The region of negative B_x and B_y coincides with reduced density and enhanced temperature, suggesting a more magnetospheric side (denoted by a blue bar on the top of Figure 2). The region of mostly positive B_x with B_y fluctuating around zero is accompanied by a density increase and a temperature decrease, representing a more magnetosheath side (red bar). Blue and red bars on the top of Figure 2 indicate repetitive excursions to the two regions by MMS. Noting that MMS was located below the equatorial plane (likely southward of the central vortex plane), the ΔB_x and ΔB_y variations across each magnetosphere-to-magnetosheath boundary (vertical dashed lines, A, B, C, and D) and magnetosheath-to-magnetosphere boundary (vertical dashed lines, a, b, c, and d) are consistent with directions of the expected engulfed magnetic field lines induced by the KHI developed at the dawn-side flank during the northward IMF (Figures 1a and 1d).

Figure 2i shows waveforms of a nonlinearly developed KHW developed along the dawnward flank magnetopause. Color coded is the electron density normalized by the initial magnetosheath value in the nonlinear growth phase of the KHW under mostly northward IMF captured from our 2–1/2-dimensional

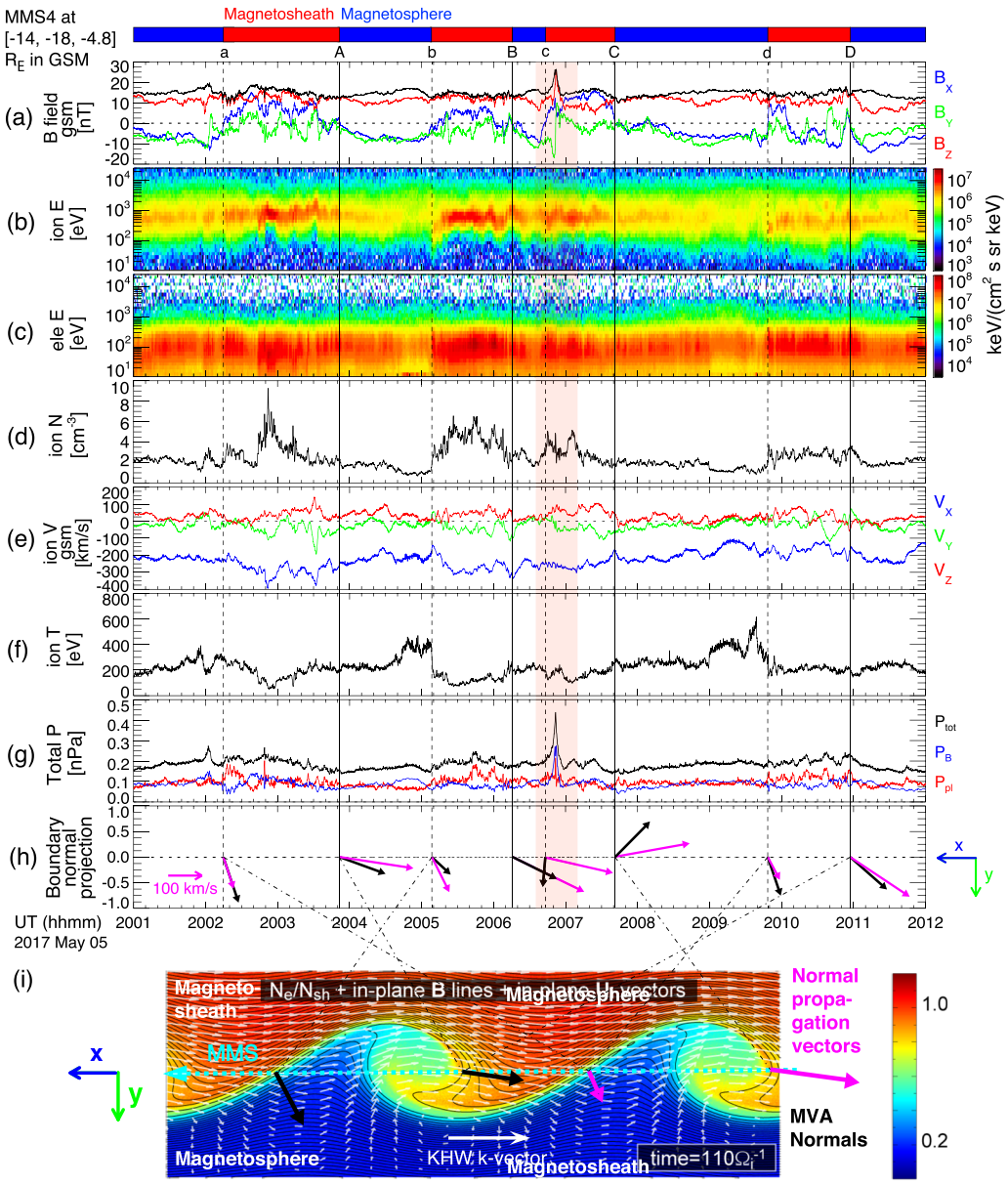

Figure 2. MMS4 observations on may 5, 2017: (a) the *l* (blue), *m* (green), and *n* (red) components of the magnetic field (**B**) in GSM; (b and c) the ion and electron energy spectrograms; (d–f) the ion density, bulk velocity, and temperature; (g) the plasma (red) and magnetic (blue) pressures, and the sum of plasma and magnetic pressures (black). Panel (h) displays the local boundary normals (black arrows) and normal propagation vectors (magenta) at the magnetosheath-to--magnetosphere (A, B, C, and D) and magnetosphere-to-magnetosheath (a, b, c, and d) the boundaries, to be compared with (i) normals and (j) normal propagation vectors for typical waveforms of a nonlinearly developed KHW, when viewed from south, with color representing temperature.

particle-in-cell (VPIC; Bowers et al., 2008) simulation (details in section 5). The snapshot shows that boundaries of the KHW in the nonlinear stage tilt from the initial undisturbed magnetopause or the initial shear flow direction (*x* direction in the simulation), forming a less tilted compressed layer at the trailing edges, i.e., low-to-high density boundaries, and a more tilted thicker mixed layer at the leading edges, i.e., high-to-low density boundaries. Since the KHI propagates tailward (−*x* in the simulation; **k**-vector seen by a white arrow in Figure 2i), the spacecraft would cross the vortex structures from right to left in Figure 2i (dashed cyan arrow). The typical waveform is, therefore, more gentle at the trailing edges (boundaries from the magnetosphere to the magnetosheath) and steeper at the leading edges (magnetosheath-to-magnetosphere crossings) (Hwang et al., 2011). Correspondingly, the boundary normals (black arrows in Figure 2i) and normal propagation velocities (magenta arrows) are more toward

Table 1
Boundary Normals and Normal Propagation Vectors at the Leading (Marked by Vertical Solid Lines, A, B, C, and D in Figure 2) and Trailing (Vertical Dashed Lines, a, b, c, and d) Edges in GSM ($\lambda_{mid\text{-}min}$ is the Medium-to-Minimum Eigenvalue Ratio in the Minimum Variance Calculation)

	a	A	b	B	c	C	d	D
Time (UT)	~20:02:15	~20:03:51	~20:05:09	~20:06:15	~20:06:42	~20:07:41	~20:09:48	~20:10:57
Normal in GSM coordinates	$\lambda_{mid\text{-}min} = 5.1$ [−0.30, 0.95, 0.05]	$\lambda_{mid\text{-}min} = 11$ [−0.91, 0.35, 0.20]	$\lambda_{mid\text{-}min} = 7.4$ [−0.38, 0.50, 0.78]	$\lambda_{mid\text{-}min} = 5.1$ [−0.88, 0.46, −0.13]	$\lambda_{mid\text{-}min} = 7.3$ [0.05, 0.62, −0.78]	$\lambda_{mid\text{-}min} = 5.0$ [−0.67, −0.74, −0.01]	$\lambda_{mid\text{-}min} = 4.9$ [−0.26, 0.81, 0.53]	$\lambda_{mid\text{-}min} = 21$ [−0.72, 0.68, 0.11]
Normal propagation in GSM	$v = 50.3$ km/s [−0.27, 0.91, 0.31]	$v = 224$ km/s [−0.98, 0.16, 0.11]	$v = 124$ km/s [−0.42, 0.88, 0.21]	$v = 240$ km/s [−0.89, 0.46, −0.03]	$v = 209$ km/s [−0.96, 0.23, −0.15]	$v = 226$ km/s [−0.98, −0.19, 0.05]	$v = 85.3$ km/s [−0.42, 0.84, 0.35]	$v = 222$ km/s [−0.79, 0.56, 0.24]

the nominal magnetopause-normal direction ($\pm y$ direction in Figure 2i) at the trailing edges. At the leading edges, they are more tangential to the nominal magnetopause surface (i.e., **k**-vector or x-direction). Owing to the alignment of normals along **k** at the leading edges, the normal propagation speed (length of magenta arrows in Figure 2i) is larger at the leading edges than at the trailing edges.

To see whether or not waveforms of the present event are consistent with this prediction, we (1) determined local normals by employing minimum variance analysis (MVA) (Sonnerup & Scheible, 1998) using **B** measured by MMS4 and (2) performed a four-spacecraft timing analysis (Paschmann & Daly, 1998) on each boundary crossing the leading (A, B, C, and D) and trailing (a, b, c, and d) edges. Table 1 lists the normal propagation velocities and the MVA-derived boundary normals together with the medium-to-minimum eigenvalue ratio averaged over spacecraft. Figure 2h displays these results as black (normals) and magenta (normal propagations) arrows at the boundaries. Both the direction of vectors and the magnitude of the normal propagation vectors show a repetitive pattern between leading and trailing edges, consistent with Figure 2i, except at "c." This confirms that the observed magnetopause fluctuations can be attributed to nonlinear KHWs or rolled-up KHVs.

For rolled-up KHVs in a steady state, the centrifugal force is balanced by the pressure force, which leads to the fact that the total pressure is minimized at the center of KHVs and maximized at the hyperbolic point (i.e., at the edge toward the magnetosheath) (Hasegawa, 2012). This signature appears around "a" and "c" (not clear around "b" and "d"). Figure 1l shows that both the sum of plasma and magnetic pressures (cyan profiles) and the sum of plasma, magnetic, and dynamic pressures (black) often peak at boundaries toward the more magnetosheath side.

Despite the overall quasi-periodicity shown in Figures 2a–2h, detailed particle signatures (Figures 2b–2f) lack discreteness across the boundary unlike dayside-magnetopause KHW events (e.g., Eriksson, Lavraud, et al., 2016), in particular, around the leading edges. The tailward plasma bulk velocity ($-V_x$ of Figure 2e) is faster in the more magnetosheath side than on the more magnetospheric side, though this becomes ambiguous toward the end of the present event. Furthermore, B_x and B_y (Figure 2a) and plasma moments (Figures 2d–2f) largely fluctuate during the magnetosheath crossings. These observations indicate that the observed KHW was highly developed (with its leading edge having multiple turnovers) or the KHW occurred at the boundary between the magnetosheath and the low-latitude boubdary layer with a relatively large density (>1 cm^{-3}).

The latter is expected for the mostly northward IMF interval (Wing et al., 2005). The former is also predicted from Figure 2i. The simulation shows that the compressed layer forms at the trailing edges (the low-to-high density boundaries when crossed by MMS) and a thicker mixed layer at the leading edges (the high-to-low density boundaries). Indeed, more rapid B_x (Figure 2a), ion density, and temperature (Figures 2d and 2f) variations were seen at the trailing edges (in particular, "b" and "d"), where the normal propagation vectors pointed close to the nominal magnetopause-normal ($\pm y$) direction. The quasi-periodic encounters of these signatures strongly indicate that MMS observed the compressed current layers located along the trailing edge of quasi-periodic KHVs.

At ~2006:50 UT near the magnetosphere-to-magnetosheath boundary, "c," we note a peak in the magnetic strength (Figure 2a) and magnetic and total pressures (Figure 2g). Simultaneously, B_y, representing a magnetic field component (B_n) normal to the nominal tail flank magnetopause, rapidly changes from negative to positive (green profile in Figure 2a within the magenta shading). The bipolar B_n with an enhanced field strength suggests that the magnetic field perturbations are associated with the overall motion of a flux rope. This localized structure may result in a notable difference between the boundary normal and the normal propagation direction at ~"c" (Figure 2h). The flux rope has been either locally formed on the trailing edge ("c") of the KHV via VIR (Nakamura et al., 2013) or has been drifting along the boundary of the observed KHW after having been generated at the dayside magnetopause. Under the strongly northward IMF previous Cluster observations combined with the prediction of Cooling et al. (2001) hardly support the latter (Fear et al., 2005). To understand the origin of the flux rope, we focus on the detailed structure of the flux rope and reconnection signatures identified within/around the flux rope in following sections.

3. The Structure of the Flux Rope

Figure 3 presents the expansion of the red shading in Figure 2 from 2006:33 UT to 2007:10 UT. Vector parameters are shown in the lmn boundary coordinate system. We determined the lmn coordinates by employing MVA using the magnetic field data for the period around the core region of the flux rope marked by two vertical lines, "I-L" and "I-T" on the top of Figure 3. To comply with conventions, m points along the axis of an flux rope, n (corresponding to MVA-l) points outward from the magnetopause, and l (MVA-n) completes the Cartesian coordinates: l = [0.91, 0.24, −0.34], m = [0.38, −0.17, 0.91], and n = [0.16, −0.96, −0.25]. The medium-to-minimum (maximum-to-medium) eigenvalue ratio is ~11.7 (10.6), indicating a reliable calculation (Siscoe & Suey, 1972). These boundary coordinates are also consistent with those obtained from both MDD (Shi et al., 2005; l = [0.90, 0.20, −0.39], m = [0.40, −0.05, 0.91], and n = [0.16, −0.98, −0.12]) and MTA (Zhou et al., 2006; l = [0.90, 0.34, −0.28], m = [0.36, −0.19, 0.91], and n = [0.26, −0.92, −0.29]) methods.

Panels of Figure 3 show (a) magnetic field (**B**), B_l, B_m, and B_n (blue, green, and red profiles), together with the magnetic strength (black); (b) electron density; (c) ion velocity ($\mathbf{V_i}$); (d) electron velocity ($\mathbf{V_e}$); (e) plasma (red) and magnetic (blue) pressures, and the sum of plasma and magnetic pressures (black); (f) parallel (blue), perpendicular (red), and total electron temperatures; (g) electric current density calculated from plasma moments; (h) electron spectrogram; (i and j) pitch angle distributions of the low- (< 200 eV), mid-(200 eV < energy <2 keV) energy electrons; (k) electric-field power spectral density (PSD). Figure 3l compares the electric-field fluctuation (δE) over three selected frequency bands derived from the PSD :$SE = \sqrt{\sum_{f_1}^{f_2} PSD \cdot \Delta f}$, where $f_1 = f_{ci}$ (ion cyclotron frequency), $f_2 = 2\, f_{LH}$ (lower hybrid frequency shown in blue in Figure 3k) for the lower hybrid band (Zhou et al., 2014) (blue); $f_1 = 0.1\, f_{ce}$, $f_2 = f_{ce}$ (the electron cyclotron frequency, black in Figure 3k) for the Whistler range (black), and $f_1 = 0.5\, f_{UH}$, $f_2 = 1.5\, f_{UH}$ (upper hybrid frequency; red in Figure 3l) for the upper hybrid range (red; based on PSD using EDP/HMFE data, not shown due to intermittency in data availability). Figures 3m and 3n show the electric field in the electron frame of reference, $\mathbf{E'} = \mathbf{E} + \mathbf{V_e} \times \mathbf{B}$ (m); Joule dissipation in the electron frame, $\mathbf{J} \cdot \mathbf{E}'$ (black in Figure 3n), decomposed into parallel and perpendicular components to **B** (blue and red profiles).

The bottom panels (Figures 3o and 3p) are obtained using the four spacecraft measurements: Figure 3o displays the current densities parallel (blue profiles) and perpendicular (red) to **B**, calculated from the curlometer technique (Dunlop et al., 2002). Figure 3p compares the l component (the largest component) of the magnetic curvature, $(\mathbf{B} \cdot \nabla \mathbf{B})/\mu_0$ (black) and the gradients of the total pressure (∇P_{tot}, green), the plasma pressure (∇P_{pl}, dotted red), and the magnetic pressure (∇P_B, dotted blue).

At ~2006:51.7 UT (the vertical black line marked by "*C*" at the top of Figure 3), i.e., at the center of the positive-to-negative B_n reversal (Figure 3a), the magnetic strength and the magnetic pressure show a local depression (black profiles in Figure 3a; blue in Figure 3e), while the total pressure increases due to enhancements of the plasma pressure (Figure 3e). This is an M-shaped crater flux rope, similar to a so-called crater flux transfer event (FTE; LaBelle et al., 1987). The B reduction at "*C*" might result from local reconnection as indicated by the out-of-plane electron jet along m (vertical green arrow in

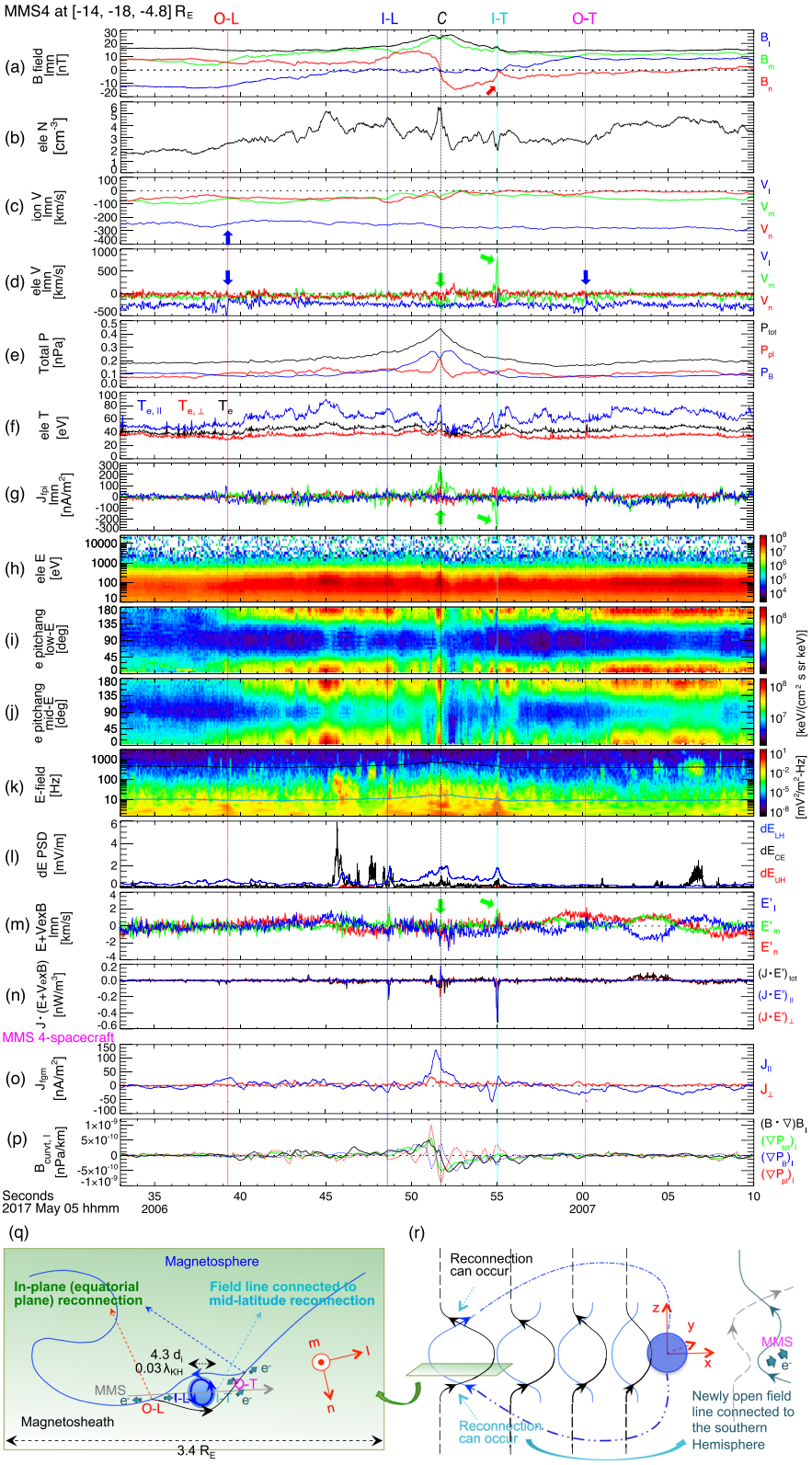

Figure 3. MMS4 observations for the expanded interval marked by the red shade of Figure 1 (details in the first three paragraphs of section 3). Panels (q and r) illustrate possible magnetic geometry in the velocity shear plane (q; viewed from north) and magnetic topology of the magnetospheric (blue in panel r) and magnetosheath fields (black) associated with midlatitude reconnection.

Figure 3d) and nonzero $\mathbf{J} \cdot \mathbf{E}'$ (3n; details in section 4). Around "*C*", the current density parallel to **B** dominates ($J_{||}$ = ~135 nA/m^2; $J_{\square perp}$= ~30 nA/m^2; 3o), suggestive of a nearly force-free flux rope ($\mathbf{J} \times \mathbf{B} = 0$; Lundquist, 1950). Around "*C*," the magnetic curvature, $(\mathbf{B} \cdot \nabla \mathbf{B})_l/\mu_0$ (black in Figure 3p) reverses its sign, as expected for the flux rope, and is largely balanced by the gradient of the total pressure, ∇P_{tot} (green). Thus, the flux rope is relatively force-balanced and not perfectly force-free ($\mathbf{J} \times \mathbf{B} = 0$, i.e., $(\mathbf{B} \cdot \nabla \mathbf{B})/\mu_0 = \nabla P_B$, where ∇P_B is shown in dotted blue in Figure 3p).

Outer boundaries denoted by "O-L" (outer leading edge) and "O-T" (outer trailing edge), denoted by the vertical red and magenta lines in Figure 3, respectively, were identified by reversals of electron velocity along *l* ($V_{e,l}$; vertical blue arrows in Figure 3d) around −250 km/s. Similar $V_{i,l}$ changes are seen at "O-L" (the blue arrow in Figure 3c) and weak fluctuations along *n* and *m* at "O-T." The $V_{i,l}$ variation changes slightly from positive ("O-L" to "*C*") to negative ("*C*" to "O-T") across "*C*." Inner boundaries, "I-L" (inner leading edge) and "I-T" (inner trailing edge) denoted by the vertical blue and cyan lines show a local dip in B_n magnitude (red arrows in Figure 3a) and a localized enhancement or reduction in the plasma density (Figure 3b) associated with the VIR-driven flux rope (Figure 5c, to be discussed in section 5). Boundary normals at these outer (inner) boundaries using MVA, MDD, and MTA methods (see Supporting Information S2), point mostly to the *n* (*l*) direction: $n_{O\text{-}L} = [0.44, -0.06, 0.90]$, $n_{I\text{-}L} = [0.78, 0.56, 0.25]$, $n_{I\text{-}T} = [0.94, -0.34, 0.01]$, and $n_{O\text{-}T} = [0.41, 0.16, 0.90]$ in lmn. These directions are consistent with the interpretation that the outer boundaries are possibly in proximity to the "anchoring" points of the outermost magnetic field lines of the flux rope; i.e., the reversals in $V_{e,l}$ may indicate in-plane reconnection occurring at the outer edges of the flux rope, from which outflowing ions ($V_{i,l}$) are ejected and converge toward the center (Hasegawa et al., 2010; Øieroset et al., 2011), and the inner boundaries may delineate the edges bounding the core region of the flux rope, as illustrated in Figure 3q.

The most distinctive feature at/around the inner boundaries is the large *m*-direction (northward) electron jet at "I-T" (slanted green arrow in Figure 3d), carrying most of the current (slanted green arrow in Figure 3g) and leading to negative $\mathbf{J} \cdot \mathbf{E}'$ (Figure 3n). Reductions in 180° pitch angle electrons (Figures 3i and 3j) indicate a reconnected field line with one end open and the other end connected to Southern Hemispheric mid-latitude reconnection (Vernisse et al., 2016; Figure 3r). The following section details these reconnection and energy conversion signatures identified within/around the flux rope.

4. Reconnection Occurring in/Around the Flux Rope

Figure 4 shows the magnetic field (a), the electron velocity (b), the pitch angle distribution of the mid-energy electrons (c), the $l_{O\text{-}L}$ components of the ion (red profiles in Figure 4d) and electron (blue) velocities perpendicular to the magnetic field compared with the $\mathbf{E} \times \mathbf{B}$ drift (black), and $\mathbf{J}\cdot\mathbf{E}'$ (d) during 2006:37–43 UT around "O-L." The boundary normal coordinates ($lmn_{O\text{-}L}$) were determined using MDD with an error indicator less than 0.1 (Supporting Information S2): $l_{O\text{-}L} = [0.81, 0.29, 0.51]$, $m_{O\text{-}L} = [-0.25, -0.62, 0.75]$, and $n_{O\text{-}L} = [0.53, -0.73, -0.43]$ in GSM.

The $V_{e,l,O\text{-}L}$ reversal (250 ± 150 km/s in Figure 4b; marked by the vertical blue line) and the reversal in $B_{l\ O\text{-}L}$ (Figure 4a; marked by the vertical black line) are separated by ~0.9 s, suggesting the displacement of the stagnant point from the X-line along the *l* direction (Hasegawa et al., 2019; Hwang et al., 2019). Around the $V_{e,l,O\text{-}L}$ reversal, the out-of-plane $V_{e,m,O\text{-}L}$ (Figure 4b) increases and the parallel heated electron flux is enhanced (red arrow in Figure 4c); $\mathbf{J}\cdot\mathbf{E}'$ is negative (Figure 4e), which represents a transfer of energy from the plasma to the fields and has been reported at the outer edge of the EDR (Hwang et al., 2017) or in association with waves (Swisdak et al., 2018; Figure 3k). After the $B_{l,O\text{-}L}$ reversal, $B_{l,O\text{-}L}$ fluctuating around 0 indicates that the spacecraft was located near the current sheet until ~2006:42 UT, during which both ion and electron velocities perpendicular to **B** somewhat deviate from $\mathbf{E} \times \mathbf{B}$ (Figure 4d). Figure 4f displays the electron distribution at ~2006:40.7 UT (denoted by the vertical magenta line) onto two perpendicular directions in 3-D velocity space: along the perpendicular component of the ion bulk velocity ($\mathbf{V}_i$), $\mathbf{V}_{\perp 1} = \mathbf{B} \times (\mathbf{V}_i \times \mathbf{B})$ and $\mathbf{V}_{\perp 2} = \mathbf{B} \times \mathbf{V}_i$. The crescent-shaped layer (magenta arrow) appears superposed onto a gyrotropic distribution throughout the interval near the current sheet, where $\mathbf{J}\cdot\mathbf{E}'$ fluctuates around 0 (Figure 4e), as well as near the $V_{e,l,O\text{-}L}$ reversal (vertical blue line in Figures 4a–4e).

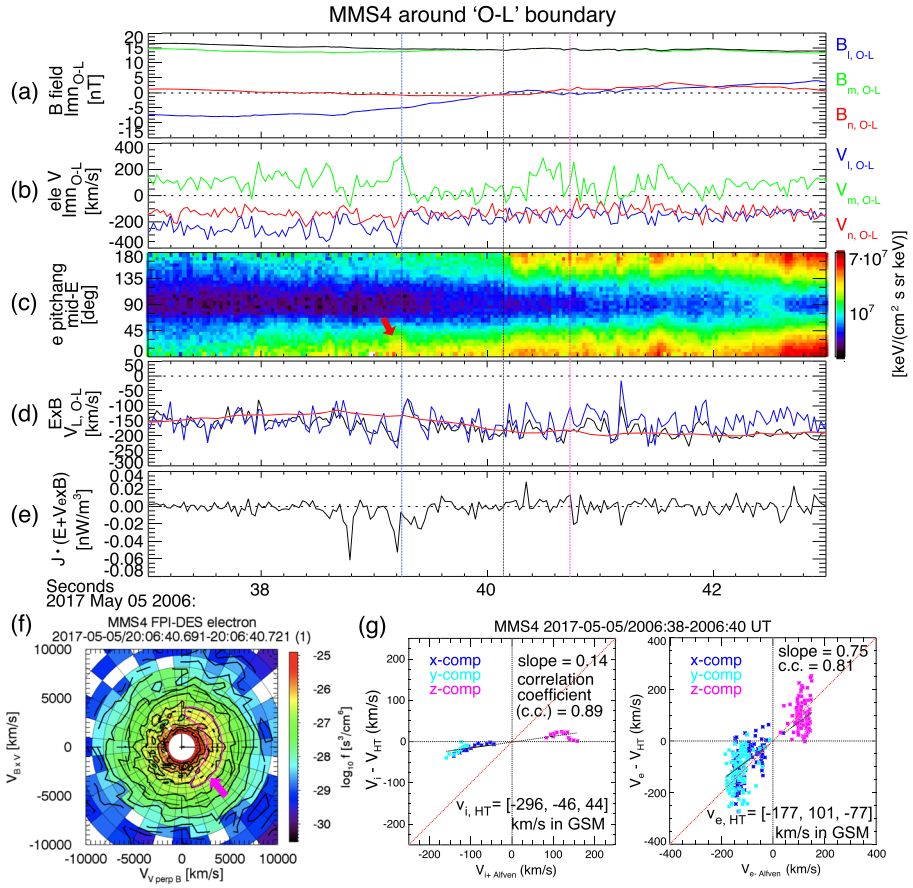

Figure 4. MMS4 observations around "O-L" shown in Figure 2a: (a) The magnetic field, (b) the electron velocity, (c) the pitch angle distribution of the midenergy electrons, (e) the $l_{O\text{-}L}$ components of the ion (red in panel d) and electron (blue) velocities perpendicular to the magnetic field compared with the $\mathbf{E} \times \mathbf{B}$ drift (black), and $\mathbf{JE}'$. Panel (f) shows the electron distribution in the ($\mathbf{V}_{\perp 1}$, $\mathbf{V}_{\perp 2}$) plane at ~2006:40.7 UT (denoted by the vertical magenta line in panels a–e). Panel (g) shows a Walén test for ions and electrons (left and right panels).

These observations, i.e., agyrotropic electron distributions (Burch, Torbert, et al., 2016), nonzero $\mathbf{J}\cdot\mathbf{E}'$, electron flow reversal and out-of-plane electron jet (Torbert et al., 2018), and electron/ion bulk motions decoupled from the magnetic field suggest active reconnection and/or a proximity to the EDR. However, these features are relatively quite weak compared to previous reports (e.g., Eriksson, Lavraud, et al., 2016; Hwang et al., 2018). Motivated by this, we performed a Walén test in the deHoffmann-Teller frame separately for ions and electrons (Hwang et al., 2016; Scudder et al., 1999) during the flow reversal (2006:38–42 UT; left and right panels of Figure 4g, where the deHoffmann-Teller velocities, $\mathbf{V}_{i,\ HT}$ and $\mathbf{V}_{e,\ HT}$ are shown). A slope of 1 is expected for current sheets undergoing reconnection. The electrons (right panel of Figure 4g) relatively satisfy the Walén test exhibiting a slope close to 1, while the ions (left panel) show a slope much less than 1. The exact same feature has been observed in proximity to an EDR (Hwang et al., 2013).

The outer tailing edge, "O-T," showing a similar electron flow reversal (Figure 3d) to "O-L," however, lacks other simultaneous signatures indicating reconnection. The $V_{e,l,O\text{-}T}$ reversal could be a signature of a separatrix connected to an active reconnection site (Phan et al., 2016; see Figure 3q near "O-T").

At the very center of the flux rope ("*C*") with the local *B* reduction (Figure 3a), the out-of-plane electron jet along -*m* (vertical green arrow in Figure 3d), which carries most of the electric current along -*m* (vertical green arrow in Figure 3g), corresponding slightly positive E_m' (vertical green arrow in Figure 3m), negligible flow reversals (Figures 3m and 3d), parallel electron heating (Figure 3f), and positive $(\mathbf{J}\cdot\mathbf{E}')_{\|}$ (Figure 3n)

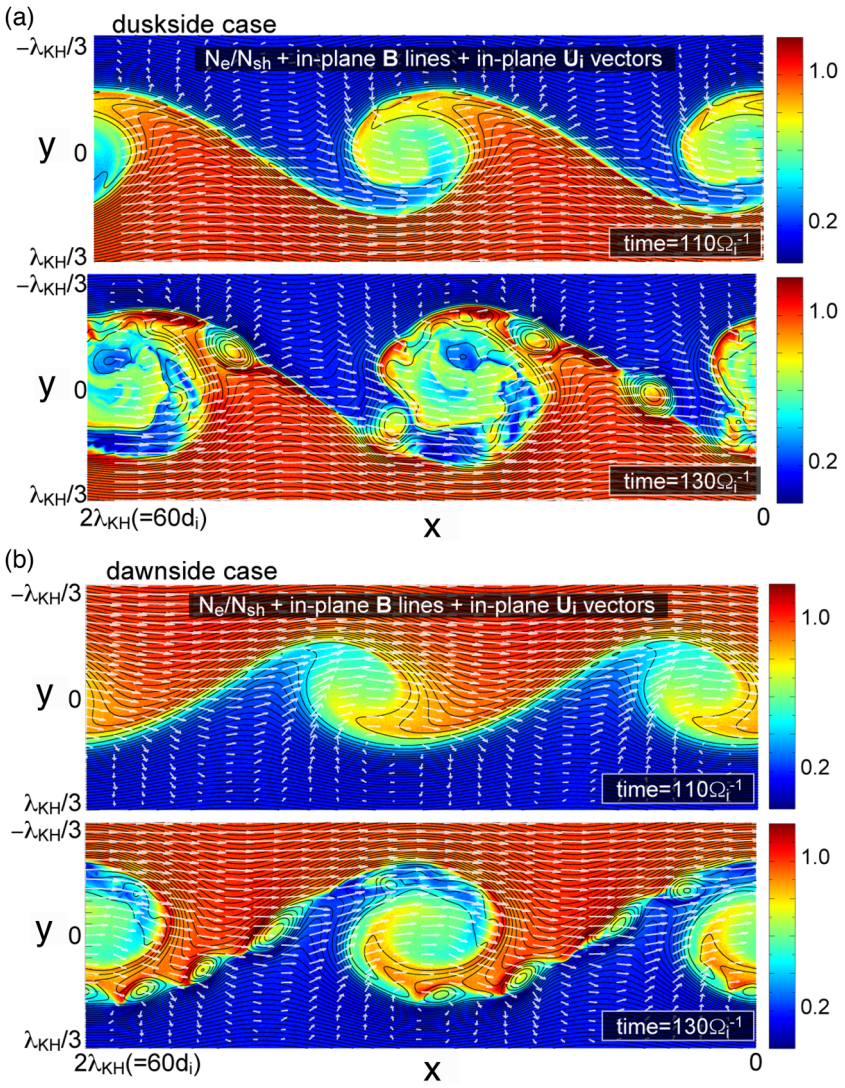

Figure 5. 2-D contours at two time slices in the non-linear growth phase of the KHI (t = 110 and 130 Ω_i^{-1}) of the electron density with the in-plane magnetic field lines and the ion flow arrows in the (a) dusk-side and (b) dawn-side cases. The coordinates in the figures are slightly changed to fit the GSM coordinates at the dusk and dawn flanks, in which x points sunward along the magnetopause, y points duskward and z points northward. The ion flow vectors (arrows) are displayed in the rest frame of the background magnetospheric plasma.

strongly suggest reconnection under a large guide field, consistent with Eriksson, Wilder, et al. (2016) and Nakamura, Hasegawa, et al. (2017).

The inner boundaries "I-L" and "I-T" are characterized by negative $\mathbf{J}\cdot\mathbf{E}'$ (Figure 3n). While notable plasma flows are absent at "I-L," "I-T" exhibits the strong northward electron jet along m, as noted in section 3 (slanted green arrow in Figure 3d). Unlike "C," $E_m{}'$ is positive (slanted green arrow in Figure 3m), indicating that the electron jets were not locally accelerated, but, resulted from a distant origin. Together with the reduction in 180° pitch angle electrons (Figures 3i and 3j), this further suggests that the magnetic field lines at "I-T" are connected to midlatitude reconnection in the Southern Hemisphere that occurred between twisted field lines of magnetosheath (black curves in Figure 3r) and magnetosphere (blue) origin.

Regarding the nonzero $\mathbf{J}\cdot\mathbf{E}'$ (Figure 3n) at the center ("C") and inner boundaries ("I-L" and "I-T"), we investigate the energy transfer occurring within the flux rope and which wave modes are responsible for the energy conversion between the fields and particles. Positive $(\mathbf{J}\cdot\mathbf{E}')_{\|}$ at "C" and negative $(\mathbf{J}\cdot\mathbf{E}')_{\|}$ at inner boundaries, in particular, "I-T" (blue profiles in Figure 3n) indicate the bulk kinetic energy transferred

from the field energy and to the field energy, respectively. Negative $(\mathbf{J}\cdot\mathbf{E}')_{\perp}$, notable at "*C*" and "I-T" (red in Figure 3n), coincides with the enhanced LH-mode wave activity (blue profiles in Figure 3l). Considering the wave propagation (almost perpendicular to **B**) expected for the LH wave, this indicates that the energy conversion, i.e., from particles to the field, occurring within the flux rope is at least partially mediated by the wave.

5. VPIC Simulation of a Flux Rope Formed Along the Boundary of KHW

We performed the first fully kinetic 2–1/2-dimensional simulation of the KHI and VIR for the dawn-side magnetopause to compare with the previous runs for the dusk-side case and the present event. We used the kinetic particle-in-cell code VPIC (Bowers et al., 2008). The initial parameters that are chosen to be comparable to the observed background magnetosheath and magnetosphere conditions (Figure 1) are similar to the previously published asymmetric layer where the initial density and magnetic and velocity shears are set up as $\mathrm{N(y)} = \frac{N_1}{2}\left[1 + tanh\left(\frac{y}{D_0}\right)\right] + \frac{N_2}{2}\left[1 - tanh\left(\frac{y}{D_0}\right)\right]$, $B_x(\mathrm{y}) = B_{x0}tanh\left(\frac{y}{D_0}\right)$, and $\mathrm{U}_x(\mathrm{y}) = \frac{V_0}{2}tanh\left(\frac{y}{D_0}\right)$ (Nakamura and Daughton (2014) for more details). Here, N_1 and $N_2 = 0.2N_1$ (compare with Figures 1h and 1j) are the initial densities of the magnetosheath and magnetosphere populations, respectively; D_0 is the half-thickness of the initial boundary layer, and V_0 is the amplitude of the initial velocity shear. To satisfy the force balance, the temperature for the magnetospheric ion component $\mathrm{T_{i2}}$ is set to be higher than the magnetosheath component T_{i1} as $T_{i2} = \frac{N_1(T_{i1}+T_e)}{N_2} - T_e$. Here, the initial electron temperature is set to be uniform and equal to $T_{\mathrm{e}} = T_{\mathrm{i1}}/3$. The guide field, corresponding to the northward field component, is set to be uniform $B_z = 5B_{x0}$ (Figure 1d). The half-thickness and the amplitude of the shear layer are set to be $D_0 = 2.0di$ and $|V_0| = 1.4V_A$, respectively, where d_i is the ion inertial length and V_A and the Alfvén speed based on N_1 and B_z. The ion-to-electron mass ratio is $m_{\mathrm{i}}/m_{\mathrm{e}} = 25$. The system size is set to be $L_{\mathrm{x}} \times L_{\mathrm{y}} = 60d_{\mathrm{i}} \times 40d_{\mathrm{i}} = 2{,}048 \times 1{,}368$ cells with a total of 1.1×10^9 superparticles. The system is periodic in *x*, and *y* boundaries are modeled as perfect conductors for the fields and reflecting for the particles. We performed two runs changing the sign of $\mathbf{V_0}$ (i.e., the direction of the velocity shear); $\mathbf{V_0} = -1.4\mathbf{V_A}$ for the dusk-side case and $\mathbf{V_0} = +1.4\mathbf{V_A}$ for the dawn-side case.

Figure 5 shows 2-D contours of the electron density at two time slices in the nonlinear growth phase of the KHI ($t = 110$ and $130\ \Omega_{\mathrm{i}}^{-1}$) in the dusk-side (Figure 5a) and dawn-side (Figure 5b) cases. In both cases, the VIR occurs at multiple points along the thin vortex edge layers compressed by the nonlinear vortex flow in the nonlinear phase, leading to the copious formation of the magnetic islands (flux ropes), as reported by past 2-D and 3-D kinetic simulations of the VIR (Nakamura et al., 2011, 2013; Nakamura & Daughton, 2014; Nakamura, Eriksson, et al., 2017; Nakamura, Hasegawa, et al., 2017). The scale sizes (peak-to-peak B_y) of the flux ropes range from $0.02\lambda_{\mathrm{KH}}$ to $0.1\lambda_{\mathrm{KH}}$ (where λ_{KH} is the wavelength of the KHW), similar to the duskward cases (Nakamura et al., 2013; Nakamura, Eriksson, et al., 2017). Although the present simulations are in 2-D, in 3-D we expect more turbulent formation and interactions of the flux ropes as shown by past 3-D simulations (Nakamura et al., 2013).

Note that the present simulation in the dawn-side case (Figure 5b) is the first fully kinetic simulation of the VIR for the dawnward magnetopause. Yet the formation mechanism and timescale of the flux ropes are nearly the same as the present (Figure 5a) and past dusk-side simulations (e.g., Nakamura et al., 2011; 2014). The half-thickness of the initial shear layer in these runs is $2d_i$, which would be rather smaller than the actual Earth's magnetopause thickness. Nonetheless, we observe a very weak dawn-dusk asymmetry, in which the KHI in the duskward case grows slightly faster than the dawnward case as reported by Nakamura et al. (2010). This asymmetry would become weaker when the initial thickness increases as predicted by Nakamura et al. (2010). These simulations clearly indicate that the VIR and the subsequent formation of the flux ropes along the trailing edge of the KHV are also expected to be seen at the dawn-side magnetopause, supporting our interpretation of the present MMS event.

6. Reconstruction of the Magnetic Field of the Flux Rope

The combined fields and plasma signatures discussed in sections 2–4 give us an overall indication of the flux rope geometry and magnetic field connectivity (Figures 3q and 3r), including coexistence of complicated substructures and multiple reconnection boundaries embedded within the flux rope. These speculations,

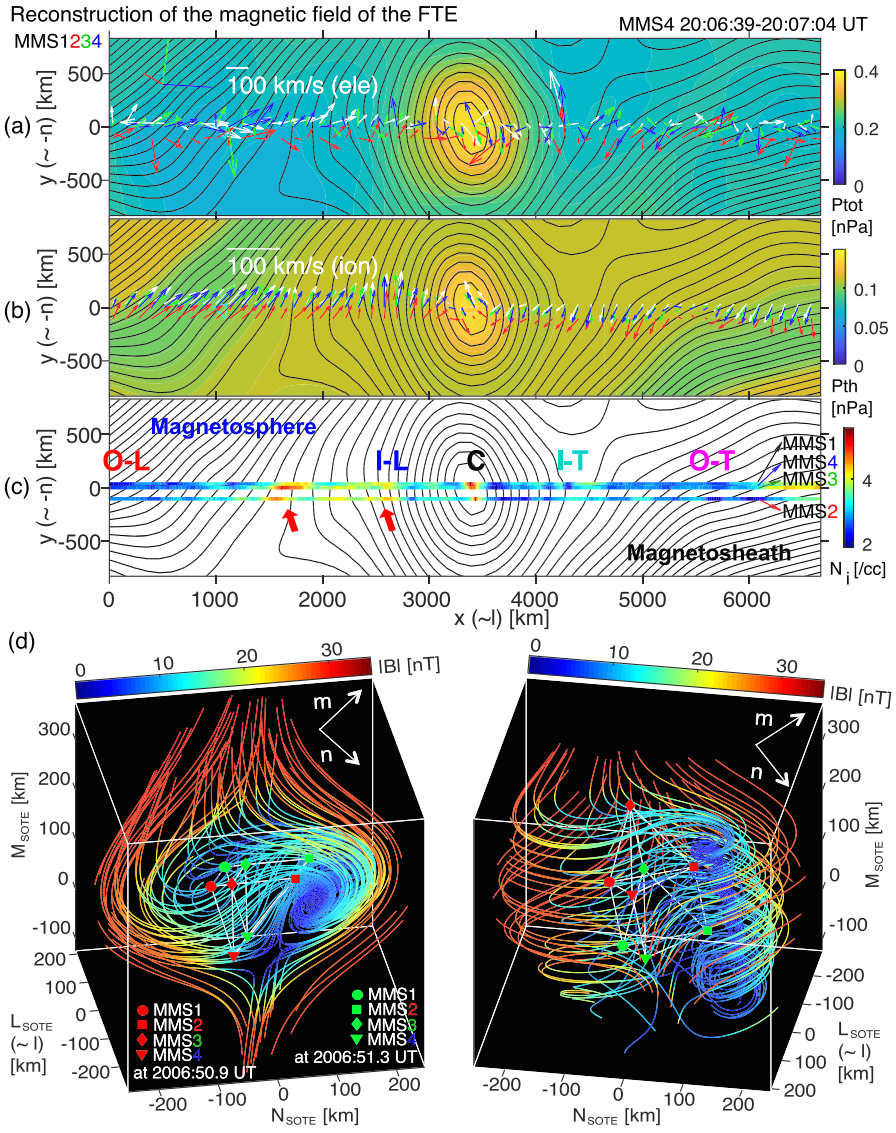

Figure 6. Results of the Grad-Shafranov (G-S) reconstruction of **B** from 2006:29 to 2017:04 UT (a–c; viewed from north) and the second-order Taylor expansion (SOTE) method around '*C*' shown in Figure 2a.

however, involve ambiguities caused by the small separation among the spacecraft as well as insufficient observations such as the lack of simultaneous reconnection signatures at "O-T." To clarify, we employ multiple reconstruction methods that advance our ability to track down the spacecraft trajectory across the flux rope.

Figures 6a–6c shows the result of the Grad-Shafranov reconstruction (Sonnerup et al., 2006; Hasegawa et al., 2006; see Supporting Information S3). This technique, although assuming 2-D and steady state, is, in particular, useful for identifying boundary structures occurring on the magnetopause and their scale sizes (see Supporting Information S3 for the validation of the 2-D assumption). The **B**-field map (black contours in Figures 6a–6c) demonstrates an elongation of the flux rope in the *y* (~−*n*) direction and ion flows (colored arrows in Figure 6b, representing MMS1, 2, 3, and 4 measurements shown in white, red, green, and blue) converging toward the flux rope center (Figure 2a), which is a typical signature when the edges of a flux rope are anchored between two X-lines (Hasegawa et al., 2010; Øieroset et al., 2011). The density variation (Figure 6c; in particular, the high density observed in the magnetosheric side—marked by the red arrows

—indicating the intrusion of the magnetosheath plasma due to the flow vortex) and a clockwise rotation of ion velocity vectors around the core (Figure 6b) are consistent with the KHV-induced flux rope (Nakamura, Hasegawa, et al., 2017). "O-L," "I-L," "*C*," "I-T," and "O-T" in Figure 3 are denoted on Figure 6c. The inner boundaries are well consistent with the reconstructed magnetic geometry, while outer boundaries only show a proximity to two X-lines inferred from the reconnection at some distance (indicating that the steady-state assumption may be not valid there). The cross-sectional distance of the peak-to-peak B_n is ~650 km (Figures 6a–6c; also, from Figure 3a using $\Delta t_{\text{p-t–p}}$, ~2.6 s and $V_{i,l}$, ~−250 km/s), which correspond to ~4.3d_i and ~0.03 λ_{KH} (the wavelength of the KHW = ~3.4 R_E, using Δt_{KH} ~87 s between "B" and "C" in Figure 2). This scaling shows excellent agreement with the predictions from our simulation shown in Figure 5b for the VIR-driven flux ropes along the dawn-side KHW and previous simulations by Nakamura et al. (2013) and Nakamura, Eriksson, et al., (2017) for the VIR-driven flux ropes along the dusk-side KHW.

The current sheet at "*C*" was suggested to undergo reconnection. Similar MMS observations have been interpreted as reconnecting current sheet between two interlinked reconnected flux tubes (Kacem et al., 2018; Øieroset et al., 2019). To reconstruct such possible 3-D magnetic field topology, we use the Taylor expansion reconstruction method up to second order by utilizing two sets of 4-point measurements of **B** at MMS1–4 (SOTE; Liu et al., 2019). This approach enables us to reconstruct nonlinear structures (e.g., two interlinked flux tubes); however, it assumes the structure to be stationary. Figure 6d shows the SOTE result around "*C*" (see Supporting Information S4). After a significant fraction (~2/3) of the background **B** has been subtracted, the core-field topology indicates two interlinked flux tubes. The interface between the two flux tubes is mostly perpendicular to the *ln* plane and their cross-section is ~400 km, corresponding to the B_n peak-to-peak distance, ~650 km.

7. Discussion and Conclusions

In this letter, we reported a VIR-induced, M-shaped crater flux rope that exhibits complicated substructures including multiple reconnection sites within/around the flux rope. Reconnection signatures identified at the outer edges (in particular, "O-L") suggest in-plane reconnection, from which converging jets toward the flux rope center compressed the core region of the flux rope. Midlatitude reconnection signatures identified at the inner trailing edge and the interacting current sheet at the very center of the flux rope indicate the 3-D structure of the KHV-induced flux rope. Using fully kinetic simulation of the VIR induced at the dawn-side magnetopause and both 2-D and 3-D reconstruction techniques, we presented the formation of the VIR-induced flux rope at the dawn-side magnetopause and both 2-D and 3-D structures of the VIR-induced flux rope that support our interpretation of the MMS observations.

Although certain types of crater-shaped FTEs have been proposed to be early stage FTEs (Zhang et al., 2012), or associated with a back-and-forth spacecraft motion relative to typical FTEs (Sibeck & Smith, 1992; Owen et al., 2008), or a separatrix crossing (Farrugia et al., 2011; Trenchi et al., 2019), their substructures and generation mechanism have not been established. The present study implies the relationship between the *B* profile of crater flux ropes and local kinetic processes occurring in the flux ropes. For example, reconnection at the center of an flux rope (Øieroset et al., 2016) or in the interface of two interlinked flux tubes (Øieroset et al., 2019; Kacem et al., 2018; Figure 5d) can result in a local dip in *B*, leading to the formation of an *M*-shaped profile of *B* (Figure 3a). At the periphery of the flux rope center, localized reconnection or magnetic tension force that radially compresses a core field can result in a *W*-shaped core profile. Testing this hypothesis requires case studies for different types of crater flux ropes to be supported by statistical studies via detailed analyses presented in this paper including force analysis (Figure 3p) and reconstruction approaches (Figure 5), which is our future study.

Acknowledgments
This study was supported, in part, by NASA's MMS project at SwRI, NSF (AGS-1834451), NASA (80NSSC18K1534, 80NSSC18K0570, 80NSSC18K0693, and 80NSSC18K1337), and ISSI program: MMS and Cluster observations of magnetic reconnection. The MMS data used for the present study are accessible through the public link provided by the MMS science working group teams: http://lasp.colorado.edu/mms/sdc/public/. We acknowledge MMS FPI and Fields teams for providing data. KJH thanks all the members of the MMS instruments and Modeling/Theory team. For the simulations employed in this paper, we acknowledge PRACE for awarding us access to MareNostrum at Barcelona Supercomputing Center (BSC), Spain.

References

Bowers, K. J., Albright, B. J., Yin, L., Bergen, B., & Kwan, T. J. T. (2008). Ultrahigh performance three-dimensional electromagnetic relativistic kinetic plasma simulations. *Physics of Plasmas*, *15*, 055703.

Burch, J. L., Moore, T. E., Torbert, R. B., & Giles, B. L. (2016). Magnetospheric multiscale overview and science objectives. *Space Science Reviews*, *199*, 5. http://doi.org/10.1007/s11214-015-0164-9

Burch, J. L., Torbert, R. B., Phan, T. D., Chen, L. J., Moore, T. E., Ergun, R. E., et al. (2016). Electron-scale measurements of magnetic reconnection in space. *Science*, *352*(6290), aaf2939. https://doi.org/10.1126/science.aaf2939

Cooling, B. M. A., Owen, C. J., & Schwartz, S. J. (2001). Role of the magnetosheath flow in determining the motion of open flux tubes. *Journal of Geophysical Research*, *106*, 18,763–18,776.

Dunlop, M., Balogh, A., Glassmeier, K.-H., & Robert, P. (2002). Four-point cluster application of magnetic field analysis tools: The Curlometer. *Journal of Geophysical Research*, *107*(A11), 1384. https://doi.org/10.1029/2001JA005088

Eriksson, S., Hasegawa, H., Teh, W. L., Sonnerup, B. U. Ö., McFadden, J. P., Glassmeier, K. H., et al. (2009). Magnetic island formation between large-scale flow vortices at an undulating postnoon magnetopause for northward interplanetary magnetic field. *Journal of Geophysical Research*, *114*, A00C17. https://doi.org/10.1029/2008JA013505

Eriksson, S., Lavraud, B., Wilder, F. D., Stawarz, J. E., Giles, B. L., Burch, J. L., et al. (2016). Magnetospheric multiscale observations of magnetic reconnection associated with Kelvin-Helmholtz waves. *Geophysical Research Letters*, *43*, 5606–5615. https://doi.org/10.1002/2016GL068783

Eriksson, S., Wilder, F. D., Ergun, R. E., Schwartz, S. J., Cassak, P. A., Burch, J. L., et al. (2016). Magnetospheric multiscale observations of the electron diffusion region of large guide field magnetic reconnection. *Physical Review Letters*, *117*(1), 015001. https://doi.org/10.1103/PhysRevLett.117.015001

Faganello, M., Califano, F., Pegoraro, F., & Andreussi, T. (2012). Double mid-latitude dynamical reconnection at the magnetopause: An efficient mechanism allowing solar wind to enter the Earth's magnetosphere. *EPL*, *100*(6), 69001. https://doi.org/10.1209/0295-5075/100/69001

Faganello, M., Califano, F., Pegoraro, F., Andreussi, T., & Benkadda, S. (2012). Magnetic reconnection and Kelvin-Helmholtz instabilities at the Earth's magnetopause. *Plasma Physics and Controlled Fusion*, *54*(12), 124,037. https://doi.org/10.1088/0741-3335/54/12/124037

Fairfield, D. H., Otto, A., Mukai, T., Kokubun, S., Lepping, R. P., Steinberg, J. T., et al. (2000). Geotail observations of the Kelvin-Helmholtz instability at the equatorial magnetotail boundary for parallel northward fields. *Journal of Geophysical Research*, *105*(A9), 21,159–21,173. https://doi.org/10.1029/1999JA000316

Farris, M. H., & Russell, C. T. (1994). Determining the standoff distance of the bow shock: Mach number dependence and use of models. *Journal of Geophysical Research*, *99*, 17,681.

Farrugia, C. J., Chen, L.-J., Torbert, R. B., Southwood, D. J., Cowley, S. W. H., Vrublevskis, A., et al. (2011). "Crater" flux transfer events: Highroad to the X line? *Journal of Geophysical Research*, *116*, A02204. https://doi.org/10.1029/2010JA015495

Fear, R. C., Fazakerley, A. N., Owen, C. J., & Lucek, E. A. (2005). A survey of flux transfer events observed by cluster during strongly northward IMF. *Geophysical Research Letters*, *32*, L18105. https://doi.org/10.1029/2005GL023811

Hasegawa, A. (1975). *Plasma Instabilities and Non-linear Effects*. New York: Springer-Verlag.

Hasegawa, H. (2012). Structure and dynamics of the magnetopause and its boundary layers. *Monographs on Environment, Earth and Planets*, *1*(2), 71–119.

Hasegawa, H., Denton, R. E., Nakamura, R., Genestreti, K. J., Nakamura, T. K. M., Hwang, K.-J., et al. (2019). Reconstruction of the electron diffusion region of magnetotail reconnection seen by the MMS spacecraft on 11 July 2017. *Journal of Geophysical Research: Space Physics*, *124*, 122–138. https://doi.org/10.1029/2018JA026051

Hasegawa, H., Fujimoto, M., Phan, T.-D., Rème, H., Balogh, A., Dunlop, M. W., et al. (2004). Transport of solar wind into Earth's magnetosphere through rolled-up Kelvin-Helmholtz vortices. *Nature*, *430*, 755.

Hasegawa, H., Sonnerup, B. U. Ö., Owen, C. J., Klecker, B., Paschmann, G., Balogh, A., & Rème, H. (2006). The structure of flux transfer events recovered from cluster data. *Annales de Geophysique*, *24*, 603–618.

Hasegawa, H., Wang, J., Dunlop, M. W., Pu, Z. Y., Zhang, Q.-H., Lavraud, B., et al. (2010). Evidence for a flux transfer event generated by multiple X-line reconnection at the magnetopause. *Geophysical Research Letters*, *37*, L16101. https://doi.org/10.1029/2010GL044219

Hwang, K.-J., Choi, E., Dokgo, K., Burch, J. L., Sibeck, D. G., Giles, B. L., et al. (2019). Electron Vorticity indicative of the Electron diffusion region of magnetic reconnection. *Geophysical Research Letters*, *46*, 6287–6296. https://doi.org/10.1029/2019GL082710

Hwang, K.-J., Goldstein, M. L., Wendel, D. E., Fazakerley, A. N., & Gurgiolo, C. (2013). Cluster observations near reconnection X lines in Earth's magnetotail current sheet. *Journal of Geophysical Research: Space Physics*, *118*, 4199–4209. https://doi.org/10.1002/jgra.50403

Hwang, K.-J., Kuznetsova, M. M., Sahraoui, F., Goldstein, M. L., Lee, E., & Parks, G. K. (2011). Kelvin-Helmholtz waves under southward interplanetary magnetic field. *Journal of Geophysical Research*, *116*, A08210. https://doi.org/10.1029/2011JA016596

Hwang, K.-J., Sibeck, D. G., Burch, J. L., Choi, E., Fear, R. C., Lavraud, B., et al. (2018). Small-scale flux transfer events formed in the reconnection exhaust region between two X lines. *Journal of Geophysical Research: Space Physics*, *123*, 8473–8488. https://doi.org/10.1029/2018JA025611

Hwang, K. -J., Sibeck, D. G., Choi, E., Chen, L. -J., Ergun, R. E., Khotyaintsev, Y., et al. (2017). Magnetospheric multiscale mission observations of the outer electron diffusion region. *Geophysical Research Letters*, *44*, 2049–2059. https://doi.org/10.1002/2017GL072830

Hwang, K.-J., Sibeck, D. G., Giles, B. L., Pollock, C. J., Gershman, D., Avanov, L., et al. (2016). The substructure of a flux transfer event observed by the MMS spacecraft. *Geophysical Research Letters*, *43*, 9434–9443. https://doi.org/10.1002/2016GL070934

Kacem, I., Jacquey, C., Génot, V., Lavraud, B., Vernisse, Y., Marchaudon, A., et al. (2018). Magnetic reconnection at a thin current sheet separating two interlaced flux tubes at the Earth's magnetopause. *Journal of Geophysical Research: Space Physics*, *123*, 1779–1793. https://doi.org/10.1002/2017JA024537

LaBelle, J., Treumann, R., Haerendel, G., Bauer, O., Paschmann, G., Baumjohann, W., et al. (1987). AMPTE IRM observations of waves associated with flux transfer events in the magnetosphere. *Journal of Geophysical Research*, *92*, 5827–5843.

Liu, Y. Y., Fu, H. S., Olshevsky, V., Pontin, D. I., Liu, C. M., Wang, Z., et al. (2019). SOTE: A nonlinear method for magnetic topology reconstruction in space plasmas. *Astrophysical Journal - Supplement Series*, *244*, 31. https://doi.org/10.3847/1538-4365/ab391a

Lundquist, S. (1950). Magnetohydrostatic fields, Ark. *Fys*, *2*, 361–365.

Nakamura, T. K. M., & Daughton, W. (2014). Turbulent plasma transport across the Earth's low-latitude boundary layer. *Geophysical Research Letters*, *41*, 8704–8712. https://doi.org/10.1002/2014GL061952

Nakamura, T. K. M., Daughton, W., Karimabadi, H., & Eriksson, S. (2013). Three-dimensional dynamics of vortex-induced reconnection and comparison with THEMIS observations. *Journal of Geophysical Research: Space Physics*, *118*, 5742–5757. https://doi.org/10.1002/jgra.50547

Nakamura, T. K. M., Eriksson, S., Hasegawa, H., Zenitani, S., Li, W. Y., Genestreti, K. J., et al. (2017). Mass and energy transfer across the Earth's magnetopause caused by vortex-induced reconnection. *Journal of Geophysical Research: Space Physics*, *122*, 11,505–11,522. https://doi.org/10.1002/2017JA024346

Nakamura, T. K. M., Hasegawa, H., Daughton, W., Eriksson, S., Li, W. Y., & Nakamura, R. (2017). Turbulent mass transfer caused by vortex induced reconnection in collisionless magnetospheric plasmas. *Nature Communications*, *8*(1), 1582. https://doi.org/10.1038/s41467-017-01579-0

Nakamura, T. K. M., Hasegawa, H., & Shinohara, I. (2010). Kinetic effects on the Kelvin-Helmholtz instability in ion-to-magnetohydrodynamic scale transverse velocity shear layer: Particle simulations. *Physics of Plasmas*, *17*, 042119. https://doi.org/10.1063/1.3385445

Nakamura, T. K. M., Hasegawa, H., Shinohara, I., & Fujimoto, M. (2011). Evolution of an MHD-scale kelvin-Helmholtz vortex accompanied by magnetic reconnection: Two-dimensional particle simulations. *Journal of Geophysical Research*, *116*, A03227. https://doi.org/10.1029/2010JA016046

Nykyri, K., & Otto, A. (2001). Plasma transport at the magnetospheric boundary due to reconnection in Kelvin-Helmholtz vortices. *Geophysical Research Letters*, *28*, 3565.

Øieroset, M., Phan, T. D., Drake, J. F., Eastwood, J. P., Fuselier, S. A., Strangeway, R. J., et al. (2019). Reconnection with magnetic flux pileup at the Interface of converging jets at the magnetopause. *Geophysical Research Letters*, *46*, 1937–1946. https://doi.org/10.1029/2018GL080994

Øieroset, M., Phan, T. D., Eastwood, J. P., Fujimoto, M., Daughton, W., Shay, M. A., et al. (2011). Direct evidence for a three-dimensional magnetic flux rope flanked by two active magnetic reconnection X lines at Earth's magnetopause. *Physical Review Letters*, *107*(16), 165,007. https://doi.org/10.1103/PhysRevLett.107.165007

Øieroset, M., Phan, T. D., Haggerty, C., Shay, M. A., Eastwood, J. P., Gershman, D. J., et al. (2016). MMS observations of large guide field symmetric reconnection between colliding reconnection jets at the center of a magnetic flux rope at the magnetopause. *Geophysical Research Letters*, *43*, 5536–5544. https://doi.org/10.1002/2016GL069166

Otto, A., & Fairfield, D. H. (2000). Kelvin-Helmholtz instability at the magnetotail boundary: MHD simulation and comparison with Geotail observations. *Journal of Geophysical Research*, *105*, 21,175.

Paschmann, G., & Daly, P. W. (1998). *Analysis methods for multispacecraft data*, Int*Space Sci. Inst., Bern*.

Owen, C. J., Marchaudon, A., Dunlop, M. W., Fazakerley, A. N., Bosqued, J.-M., Dewhurst, J. P., et al. (2008). Cluster observations of "crater" flux transfer events at the dayside high-latitude magnetopause. *Journal of Geophysical Research*, *113*, A07S04. https://doi.org/10.1029/2007JA012701

Phan, T. D., Eastwood, J. P., Cassak, P. A., Øieroset, M., Gosling, J. T., Gershman, D. J., et al. (2016). MMS observations of electron-scale filamentary currents in the reconnection exhaust and near the X line. *Geophysical Research Letters*, *43*, 6060–6069. https://doi.org/10.1002/2016GL069212

Scudder, J. D., Puhl-Quinn, P. A., Mozer, F. S., Ogilvie, K. W., & Russell, C. T. (1999). Generalized Walén tests through Alfvén waves and rotationaldiscontinuities using electron flow velocities. *Journal of Geophysical Research*, *104*, 19817–19834. https://doi.org/10.1029/1999JA900146

Shi, Q. Q., Shen, C., Pu, Z. Y., Dunlop, M. W., Zong, Q.-G., Zhang, H., et al. (2005). Dimensional analysis of observed structures using multipoint magnetic field measurements: Application to cluster. *Geophysical Research Letters*, *32*, L12105. https://doi.org/10.1029/2005GL022454

Sibeck, D. G., & Smith, M. F. (1992). Magnetospheric plasma flows associated with boundary waves and flux transfer events. *Geophysical Research Letters*, *19*(19), 1903–1906. https://doi.org/10.1029/92GL01614

Siscoe, G. L., & Suey, R. W. (1972). Significance criteria for variance matrix applications. *Journal of Geophysical Research*, *77*, 1321–1322. https://doi.org/10.1029/JA077i007p01321

Sonnerup, B. U. Ö., Hasegawa, H., Teh, W.-L., & Hau, L.-N. (2006). Grad-Shafranov reconstruction: An overview. *Journal of Geophysical Research*, *111*, A09204. https://doi.org/10.1029/2006JA011717

Sonnerup, B. U. Ö., & Scheible, M. (1998). Minimum and maximum variance analysis. *ISSI Scientific Report*, *1*, 185–220.

Swisdak, M., Drake, J. F., Price, L., Burch, J. L., Cassak, P. A., & Phan, T. D. (2018). Localized and intense energy conversion in the diffusion region of asymmetric magnetic reconnection. *Geophysical Research Letters*, *45*, 5260–5267. https://doi.org/10.1029/2017GL076862

Takagi, K., Hashimoto, C., Hasegawa, H., Fujimoto, M., & TanDokoro, R. (2006). Kelvin-Helmholtz instability in a magnetotail flank-like geometry: Three-dimensional MHD simulations. *Journal of Geophysical Research*, *111*, A08202. https://doi.org/10.1029/2006JA011631

Torbert, R. B., Burch, J. L., Phan, T. D., Hesse, M., Argall, M. R., Shuster, J., et al. (2018). Electron-scale dynamics of the diffusion region during symmetric magnetic reconnection in space. *Science*, *362*(6421), 1391–1395. https://doi.org/10.1126/science.aat2998

Trenchi, L., Coxon, J. C., Fear, R. C., Eastwood, J. P., Dunlop, M. W., Trattner, K. J., et al. (2019). Signatures of magnetic separatrices at the borders of a crater flux transfer event connected to an active X-line. *Journal of Geophysical Research: Space Physics*, *124*, 8600–8616. https://doi.org/10.1029/2018JA026126

Vernisse, Y., Lavraud, B., Eriksson, S., Gershman, D. J., Dorelli, J., Pollock, C., et al. (2016). Signatures of complex magnetic topologies from multiple reconnection sites induced by Kelvin-Helmholtz instability. *Journal of Geophysical Research: Space Physics*, *121*, 9926–9939. https://doi.org/10.1002/2016JA023051

Wing, S., Johnson, J. R., Newell, P. T., & Meng, C.-I. (2005). Dawn-dusk asymmetries, ion spectra, and sources in the northward interplanetary magnetic field plasma sheet. *Journal of Geophysical Research*, *110*, A08205. https://doi.org/10.1029/2005JA011086

Zhang, H., Kivelson, M. G., Angelopoulos, V., Khurana, K. K., Pu, Z. Y., Walker, R. J., et al. (2012). Generation and properties of in vivo flux transfer events. *Journal of Geophysical Research*, *117*, A05224. https://doi.org/10.1029/2011JA017166

Zhou, M., Li, H., Deng, X., Huang, S., Pang, Y., Yuan, Z., et al. (2014). Characteristic distribution and possible roles of waves around the lower hybrid frequency in the magnetotail reconnection region. *Journal of Geophysical Research: Space Physics*, *119*, 8228–8242. https://doi.org/10.1002/2014JA019978

Zhou, X.-Z., Zong, Q.-G., Pu, Z. Y., Fritz, T. A., Dunlop, M. W., Shi, Q. Q., et al. (2006). Multiple triangulation analysis: Another approach to determine the orientation of magnetic flux ropes. *Annales de Geophysique*, *24*, 1759–1765. http://www.ann-geophys.net/24/1759/2006/

References From the Supporting Information

Ergun, R. E., Tucker, S., Westfall, J., Goodrich, K. A., Malaspina, D. M., Summers, D., et al. (2014). The axial double probe and fields signal processing for the MMS Mission. *Space Science Reviews*, *199*(1–4), 167–188. https://doi.org/10.1007/s11214-014-0115-x

Khrabrov, A. V., & Sonnerup, B. U. Ö. (1998). DeHoffmann-teller analysis. In G. Paschmann, & P. W. Daly (Eds.), *Analysis methods for multispacecraft data* (Chap. 9, (pp. 221–248). Bern, Switzerland: Int. Space Sci. Inst.

Lindqvist, P.-A., Olsson, G., Torbert, R. B., King, B., Granoff, M., Rau, D., et al. (2016). The spin-plane double probe electric field instrument for MMS. *Space Science Reviews*, *199*(1–4), 137–165. https://doi.org/10.1007/s11214-014-0116-9

Pollock, C., Moore, T., Jacques, A., Burch, J., Gliese, U., Saito, Y., et al. (2016). Fast plasma investigation for magnetospheric multiscale. *Space Science Reviews*, *199*(1–4), 331–406. https://doi.org/10.1007/s11214-016-0245-4

Russell, C. T., Anderson, B. J., Baumjohann, W., Bromund, K. R., Dearborn, D., Fischer, D., et al. (2016). The magnetospheric multiscale magnetometers. *Space Science Reviews*, *199*(1–4), 189–256. https://doi.org/10.1007/s11214-014-0057-3